

Photoacoustic tomography with time-dependent damping: Theoretical and a convolutional neural network-guided numerical inversion procedure

Sunghwan Moon^a, Anwesa Dey^b, and Souvik Roy^c

^a Department of Mathematics, Kyungpook National University, Daegu 41566, Republic of Korea

^b Department of Mathematics, University of Utah, Salt Lake City, UT 84112, USA

^c Department of Mathematics, The University of Texas at Arlington, Arlington, TX 76019, USA

Abstract

In photoacoustic tomography (PAT), a hybrid imaging modality that is based on the acoustic detection of optical absorption from biological tissue exposed to a pulsed laser, a short pulse laser generates an initial pressure proportional to the absorbed optical energy, which then propagates acoustically and is measured on the boundary. To account for the significant signal distortion caused by acoustic attenuation in biological tissue, we model PAT in heterogeneous media using a damped wave equation featuring spatially varying sound speed and a time-dependent damping term. Under natural assumptions, we show that the initial pressure is uniquely determined by the boundary measurements using a harmonic extension of the boundary data with energy decay. For constant damping, an expansion in Dirichlet eigenfunctions of $-c^2(\mathbf{x})\Delta$ leads to an explicit series reconstruction formula for the initial pressure. Finally, we develop a gradient free numerical method based on the Pontryagin's maximum principle to provide a robust and computationally viable approach to image reconstruction in attenuating PAT.

keywords: Wave equation, time-dependent damping, photoacoustic tomography, optimization, inversion

MSCcodes: 35R30, 35L05, 49J20, 49K20

1 Introduction

Optical tomography (OT) is a biomedical imaging modality that exploits the propagation of light in the near-infrared (NIR) spectral range to reconstruct the optical properties of biological media, such as tissues. Since malignant tissue typically scatters light less than healthy tissue, accurate recovery of spatially varying scattering and absorption coefficients is essential for reliable cancer diagnosis. However, the inverse problem in OT is severely ill-posed and, in practice, often leads to reconstructions with poor spatial resolution. To overcome these limitations and obtain high-fidelity maps of optical parameters, a variety of multi-physics imaging techniques, such as fluorescence molecular tomography, confocal diffuse tomography, single-photon photoacoustic tomography, two-photon photoacoustic tomography, and ultrasound-modulated optical tomography, have been developed under the umbrella of hybrid OT methods (see, e.g., [4, 14, 19]). Among these, photoacoustic tomography (PAT) [18, 42, 44] has emerged as

one of the most prominent approaches owing to its wide range of biomedical applications. Consequently, the development of accurate and efficient computational models for image reconstruction in PAT is of considerable importance.

In PAT, a heterogeneous object, typically biological tissue, is illuminated along its boundary by short pulses of NIR light. As photons propagate through the medium, a fraction of the optical energy is absorbed, causing localized heating and subsequent thermoelastic expansion of the tissue, while the remaining photons undergo multiple scattering events. After the illumination ceases, the tissue cools and contracts. This sequence of rapid expansion and contraction generates transient pressure variations inside the object, which in turn produce acoustic (ultrasound) waves through the photoacoustic effect [9]. These pressure waves propagate outward and are recorded by ultrasound detectors positioned on (or near) the surface of the object. Acoustic propagation in tissue occurs on microsecond time scales, which are roughly three orders of magnitude slower than optical diffusion. The core mathematical task in PAT is an inverse problem: reconstructing the initial pressure distribution, which is proportional to the absorbed optical energy density, from the measured acoustic signals at the boundary (see, for instance, [5, 7, 30, 45] and the references therein).

Many mathematical studies on PAT model the pressure field by the standard wave equation with a variable sound speed; see, for instance, [22, 26, 28, 31, 32] and the references therein. Although such models capture the finite-speed propagation and heterogeneity of sound speed reasonably well, they neglect the attenuation mechanisms that are intrinsic to biological tissue. In reality, as pressure waves travel through the medium, their amplitudes are gradually reduced due to absorption, scattering, and viscous losses. This attenuation can significantly influence the measured signals and, if not appropriately accounted for, may lead to systematic reconstruction artifacts and loss of resolution. To address this issue, several attenuation models have been proposed in the PAT literature [6, 16, 27, 29, 33], including frequency-power-law models, thermo-viscous models, and more general convolution-in-time formulations; the corresponding inverse problems are typically more challenging and may suffer from increased ill-posedness. Moreover, most of these models are formulated under the simplifying assumption of a constant sound speed.

In this work, we focus on a time-dependent damped wave equation in PAT. Specifically, we consider the pressure field $p(\mathbf{x}, t)$ as the solution to the Cauchy problem

$$\partial_t^2 p(\mathbf{x}, t) + \gamma(t) \partial_t p(\mathbf{x}, t) - c(\mathbf{x})^2 \Delta p(\mathbf{x}, t) = 0, \quad (\mathbf{x}, t) \in \mathbb{R}^n \times [0, \infty), \quad (1)$$

where $n \in \mathbb{N}$ denotes the spatial dimension, with the initial data

$$p(\mathbf{x}, 0) = p_0(\mathbf{x}), \quad \partial_t p(\mathbf{x}, 0) = 0. \quad (2)$$

Here, $c(\cdot)$ denotes a spatially varying sound speed and $\gamma(\cdot) > 0$ is a smooth, strictly positive damping function that models cumulative attenuation phenomena such as absorption and viscous losses. We assume that the region of interest $\Omega \subset \mathbb{R}^n$ is a bounded domain with smooth boundary $\partial\Omega$ and that the sound speed, the damping coefficient, and the initial data satisfy the assumptions (3) stated in Section 2. The measured data are given by the boundary trace

$$g(\mathbf{y}, t) = p(\mathbf{y}, t) \Big|_{(\mathbf{y}, t) \in \partial\Omega \times [0, \infty)}.$$

In this paper, we study how to reconstruct the initial pressure distribution p_0 , and hence the absorbed optical energy density, inside Ω from the knowledge of g .

We also note that, when the damping coefficient in (1) depends only on space, $\gamma = \gamma(\mathbf{x})$, related inverse problems have been studied in the literature [15, 23, 24, 36]. For variable sound speed $c(\cdot)$ the inverse problem can be treated by time-reversal based reconstruction/the Neumann series reconstruction [25, 34, 35, 43], and in [23] this approach was further extended to the case of spatially dependent damping. In the context of multiwave imaging, Homan [24] and Palacios [36] analyzed damped wave equations with spatially varying attenuation and derived Neumann-series-type reconstruction formulas under suitable assumptions. However, in the presence of time-dependent damping the underlying time-reversal symmetry is lost, and such time-reversal techniques no longer apply in a straightforward way.

Our first contribution is an analytical study of the inverse problem for the time-dependent damped wave equation (1). Under assumptions of natural regularity and boundedness in c and γ , we construct an auxiliary field u satisfying homogeneous Dirichlet conditions on $\partial\Omega$ whose energy decays in time. Following the eigenfunction-expansion framework based on harmonic extension and Dirichlet eigenfunctions that was originally employed in the PAT context by Agranovsky and Kuchment [2], we introduce the harmonic extension operator E from $\partial\Omega$ into Ω and expand the unknown field in terms of Dirichlet eigenfunctions $\{\psi_k\}_{k \in \mathbb{N}}$ of the elliptic operator $-c(\mathbf{x})^2\Delta$. On this frame, we establish that the initial pressure distribution p_0 is uniquely determined by the boundary measurements g on $\partial\Omega \times [0, \infty)$, thus providing a uniqueness result for the PAT inverse problem in the presence of a general time-dependent damping term.

Our second contribution is an explicit inversion procedure in the special but practically relevant case where the damping coefficient is constant, $\gamma(t) = \gamma > 0$. Using the harmonic extension operator and the unknown field in terms of Dirichlet eigenfunctions, the damped wave equation is reduced to a family of decoupled second-order ordinary differential equations for the coefficients. For constant γ , these ODEs can be solved explicitly, which yields closed-form expressions for the coefficients of u and, consequently, for $p_0 - Eg(\cdot, 0)$ in terms of time-convolutions of the measured data g and its time derivatives. This leads to an analytic series reconstruction formula for p_0 inside Ω in the weighted space $L^2(\Omega, c^{-2})$.

For the numerical reconstruction of the initial pressure p_0 , we aim to minimize a Tikhonov-type least-squares functional that incorporates data fitting terms and sparsity-promoting regularization terms. While the inclusion of nonsmooth regularization significantly enhances the method's ability to produce sharp reconstructions, as demonstrated in [1, 39], it also necessitates advanced optimization techniques suitable for nonsmooth settings, two of which are proximal methods and semi-smooth Newton (SSN) methods [8, 20, 21]. However, implementing these approaches requires evaluating the subgradients and Hessian of the optimization problem, which involves solving not only the state and adjoint equations but also two additional linearized systems. These requirements, together with other implementation challenges, render these schemes demanding for practical use.

To address these challenges, we use the sequential quadratic Hamiltonian (SQH) algorithm, which was originally proposed in [11, 12, 13] for nonsmooth PDE-constrained optimal control problems, to our inverse problem. The SQH method is grounded in the Pontryagin maximum principle (PMP), a cornerstone of optimal control theory. We are particularly motivated by the SQH algorithm's ease of implementation, strong efficiency and robustness, and well-posedness as an iterative scheme [12, 13]. A distinctive feature of this iterative approach is its reliance on a pointwise optimization procedure. Such a scheme has been recently used in context of tomographic inverse problems arising in optical tomography [14, 38, 40, 41]. However, since the SQH method is iterative, its performance depends heavily on initial guesses. Traditional options are to either provide a specified initial guess, like 0, or construct an approximate solution using some other algorithm and use that as the initial guess. It is worthwhile to note that iterative algorithms like SQH work better if the structure of the initial guess resembles the

structure of the true solution. One viable approach would be to use the time-reversal algorithm and obtain an approximation of p_0 , to be used as an initial guess. However, even though the time-reversal algorithm might be able to avoid appearance of spurious discontinuities or violate the underlying physics, due to the structure of the attenuated wave equation, there will be significant damping, resulting in huge loss of contrast.

On the other hand, convolutional neural networks (CNNs) have proven highly effective for recovering parameters in ill-posed, PDE-constrained inverse problems. The CNNs learn directly from data. Their data-driven nature allows them to extract complex, problem-specific features that would be difficult or even impossible to encode analytically as explicit priors. Moreover, CNNs are well suited for representing nonlinear relationships: by stacking convolution operations, which are linear, with nonlinear activation functions, they build hierarchical representations capable of approximating highly nonlinear mappings between inputs and outputs. This interplay of layered convolutions and nonlinear activations enables CNNs to model intricate structures that arise in challenging inverse problems. Furthermore, unlike classical optimization-based approaches, where regularization must be introduced explicitly through penalty terms such as L^2, L^1 , or Tikhonov regularization, CNNs embed regularization implicitly within their architecture and training dynamics.

However, one major drawback of CNN (or in general any traditional deep learning algorithm) is the inability to incorporate the underlying physical structure of the problem and relies on training with a huge dataset to provide meaningful inference, especially for complex inverse problems that usually appear with PDEs. There have been some progress made in the field of machine learning through the development of physics-informed neural networks (PINN), but it still struggles to find a balance between learning patterns from data and satisfying physical constraints. Thus, the output of CNN, in general, can suffer from spurious artifacts.

In an attempt to circumvent this issue, we combine the advantages of time-reversal and CNN to choose a initial guess of our SQH as the sum of the two outputs. This ensures that the initial guess preserves some information of the discontinuities present as well as provide better starting contrast. As we will note in the results in Section 4, such a choice of initial guess guides the SQH algorithm to provide superior contrast and resolution reconstructions.

The remainder of the paper is organized as follows. In Section 2, we present the analytical framework for the damped wave equation, including well-posedness and decay estimates, and we derive the uniqueness result for the initial pressure as well as an explicit inversion formula in the case of constant damping. In Section 3, we introduce the optimization framework for solving the initial pressure numerically. The framework comprises of a cost functional with data-fitting and regularization terms. We characterize the minimizer using the PMP, and describe the SQH-based reconstruction algorithm, guided by an initial guess obtained using a CNN, for the numerical PMP implementation along with results for the convergence of the algorithm. In Section 4, we discuss the results of the reconstruction with our proposed algorithm and compare our outputs with the time-reversal algorithm, both qualitatively and quantitatively. We conclude the paper with a section of conclusions.

2 Analysis of the damped wave model

In this section we study the Cauchy problem (1)–(2) introduced in Section 1. Throughout the paper we impose the following standing assumptions on γ , c , p_0 , and the bounded domain $\Omega \subset \mathbb{R}^n$ with smooth

boundary $\partial\Omega$: for $\nu \in \mathbb{N}, \nu > n/2 + 1$,

- $\gamma(\cdot) \in C^{\nu+1}([0, \infty))$ with $0 < \gamma_m \leq \gamma(t) \leq \gamma_M$,
 - $c(\cdot) \in C^{\nu+1}(\mathbb{R}^n)$ with $0 < c_m \leq c(\mathbf{x}) \leq c_M$,
 - $p_0 \in H^\nu(\mathbb{R}^n)$ with compact support,
 - $\Omega \subset \mathbb{R}^n$ is an open and bounded domain with smooth boundary $\partial\Omega$.
- (3)

We notice that every scalar hyperbolic equation of second order can be transformed into a symmetric hyperbolic system (see [37, page 21]). Hence by Theorem 3.3 in [37], the initial problem (1) with $p(\mathbf{x}, 0) = p_0(\mathbf{x}), \partial_t p(\mathbf{x}, 0) = 0$ under assumption (3) has a unique solution $p \in C^2([0, \infty) \times \mathbb{R}^n)$ and

$$p \in C^1([0, \infty); H^\nu(\mathbb{R}^n) \cap C^2([0, \infty); H^{\nu-1}(\mathbb{R}^n))),$$

where $H^\nu(\mathbb{R}^n), \nu \in \mathbb{R}$ is the Sobolev space.

Let E denote the harmonic extension operator from $\partial\Omega$ to Ω , that is, the operator which produces a harmonic function $E\phi$ in Ω for given Dirichlet data ϕ on $\partial\Omega$. By standard regularity theory, E is continuous from $H^s(\partial\Omega)$ to $H^{s+1/2}(\Omega)$ for any $s > 0$. Hence we can rewrite (1) in terms of $u = p - Eg$ as follows:

$$\begin{aligned} \partial_t^2 u(\mathbf{x}, t) + \gamma(t)\partial_t u(\mathbf{x}, t) - c(\mathbf{x})^2 \Delta u(\mathbf{x}, t) &= -G_\gamma(\mathbf{x}, t) \\ \text{for } (\mathbf{x}, t) \in \Omega \times [0, \infty) & \\ u(\mathbf{x}, 0) = p_0(\mathbf{x}) - Eg(\mathbf{x}, 0) \quad \text{and} \quad \partial_t u(\mathbf{x}, 0) = 0 &\quad \text{for } \mathbf{x} \in \Omega \\ u(\mathbf{y}, t) = 0 \quad (\mathbf{y}, t) \in \partial\Omega \times [0, \infty), & \end{aligned} \tag{4}$$

where $G_\gamma(\mathbf{x}, t) = E(\partial_t^2 g)(\mathbf{x}, t) + \gamma(t)E(\partial_t g)(\mathbf{x}, t)$.

Let $\{\lambda_k^2, \psi_k\}_{k=1}^\infty$ be the eigenvalues and an associated orthonormal basis of eigenfunctions of the operator $-c(\mathbf{x})^2 \Delta$ with Dirichlet boundary conditions, where $\lambda_k > 0$ for all k . We use the notation

$$f_k := \langle f, \psi_k \rangle, u_k(t) := \langle u(\cdot, t), \psi_k \rangle, \quad \text{and} \quad G_{\gamma,k}(t) := \langle G_\gamma(\cdot, t), \psi_k \rangle$$

for the Fourier coefficients of f and u with respect to $\{\psi_k\}$. Here $\langle \cdot, \cdot \rangle$ denotes the inner product in $L^2(\Omega, c^{-2})$.

Theorem 1. *Under assumptions (3), the initial function $p_0(\mathbf{x}) - Eg(\mathbf{x}, 0)$ can be uniquely determined from $Eg(\mathbf{x}, t)$. Furthermore, $p_0(\mathbf{x})$ can be uniquely determined from g .*

To establish the above uniqueness result and to prepare for an explicit reconstruction formula, we expand the solution in the eigenbasis of the operator $-c(\mathbf{x})^2 \Delta$ and study the time evolution of the corresponding modal coefficients. The following lemma provides that (4) satisfies these coefficients.

Lemma 2. *If for any $k \in \mathbb{N}$, u_k satisfies*

$$u_k''(t) + \gamma(t)u_k'(t) + \lambda_k^2 u_k(t) = -G_{\gamma,k}(t), \tag{5}$$

then $L^2(\Omega, c^{-2})$ -convergent series $u = \sum u_k \psi_k$ satisfies the PDE in (4).

Proof. For any $k \in \mathbb{N}$, let us consider

$$\begin{aligned} \int_{\Omega} \Delta_{\mathbf{x}} u(\mathbf{x}, t) \overline{\psi_k(\mathbf{x})} d\mathbf{x} &= \int_{\Omega} u(\mathbf{x}, t) \Delta_{\mathbf{x}} \overline{\psi_k(\mathbf{x})} d\mathbf{x} + \int_{\partial\Omega} \partial_\nu u(\mathbf{y}, t) \overline{\psi_k(\mathbf{y})} - u(\mathbf{y}, t) \partial_\nu \overline{\psi_k(\mathbf{y})} ds(\mathbf{y}) \\ &= - \int_{\Omega} u(\mathbf{x}, t) \lambda_k^2 \overline{\psi_k(\mathbf{x})} c(\mathbf{x})^{-2} d\mathbf{x}, \end{aligned}$$

where ∂_ν is the normal derivative on $\partial\Omega$, $ds(\mathbf{y})$ denotes the surface measure on $\partial\Omega$ and $\bar{z}, z \in \mathbb{C}$, is the complex conjugate of z . Here in the first equality, we used the Green's theorem and we used the fact that u and ψ_k in $\partial\Omega$ are equal to 0 in the second equality. Multiplying the PDE in (4) by ψ_k and integrating over Ω with weight $c(\mathbf{x})^{-2}$, we have

$$\begin{aligned} -G_{\gamma,k}(t) &= \int_{\Omega} \{(\partial_t^2 + \gamma(t)\partial_t - c(\mathbf{x})^2\Delta_{\mathbf{x}})u(\mathbf{x}, t)\} \overline{\psi_k(\mathbf{x})} c(\mathbf{x})^{-2} d\mathbf{x} \\ &= \int_{\Omega} \{(\partial_t^2 + \gamma(t)\partial_t + \lambda_k^2)u(\mathbf{x}, t)\} \overline{\psi_k(\mathbf{x})} c(\mathbf{x})^{-2} d\mathbf{x}. \end{aligned}$$

Hence if for any $k \in \mathbb{N}$ u_k satisfies (5), then by the completeness of ψ_k in $L^2(\Omega, c^{-2})$ $L^2(\Omega, c^{-2})$ -convergent series u satisfies the PDE in (4). \square

To prove Theorem, we need the following proposition:

Proposition 3. *Under assumptions (3), there exists a unique global solution u of (4) such that*

$$\lim_{t \rightarrow \infty} u(\mathbf{x}, t) = \lim_{t \rightarrow \infty} \partial_t u(\mathbf{x}, t) = 0 \quad \text{for a.e. } \mathbf{x} \in \Omega. \quad (6)$$

Proof. Let us start with energy function:

$$E_{\text{total},u}(t) = \frac{1}{2} \int_{\Omega} (c(\mathbf{x})^{-2} |\partial_t u(\mathbf{x}, t)|^2 + |\nabla u(\mathbf{x}, t)|^2) d\mathbf{x}.$$

Multiplying the PDE in (4) by $\partial_t u$ and integrating over Ω , we obtain:

$$\begin{aligned} &\int_{\Omega} c(\mathbf{x})^{-2} \partial_t^2 u(\mathbf{x}, t) \partial_t u(\mathbf{x}, t) d\mathbf{x} + \int_{\Omega} \frac{\gamma(t)}{c(\mathbf{x})^2} |\partial_t u(\mathbf{x}, t)|^2 d\mathbf{x} \\ &\quad - \int_{\Omega} \Delta u(\mathbf{x}, t) \partial_t u(\mathbf{x}, t) d\mathbf{x} = - \int_{\Omega} c(\mathbf{x})^{-2} G_{\gamma}(\mathbf{x}, t) \partial_t u(\mathbf{x}, t) d\mathbf{x}. \end{aligned}$$

With Green's theorem

$$\int_{\Omega} \nabla u(\mathbf{x}) \cdot \nabla v(\mathbf{x}) d\mathbf{x} = - \int_{\Omega} u(\mathbf{x}) \Delta v(\mathbf{x}) d\mathbf{x} + \int_{\partial\Omega} u(\mathbf{y}) \partial_\nu v(\mathbf{y}) ds(\mathbf{y}), \quad (7)$$

this gives:

$$\frac{d}{dt} E_{\text{total},u}(t) + \int_{\Omega} \frac{\gamma(t)}{c(\mathbf{x})^2} |\partial_t u(\mathbf{x}, t)|^2 d\mathbf{x} = - \int_{\Omega} c(\mathbf{x})^{-2} G_{\gamma}(\mathbf{x}, t) \partial_t u(\mathbf{x}, t) d\mathbf{x}.$$

and thus with Young's inequality, we have

$$\begin{aligned} \frac{d}{dt} E_{\text{total},u}(t) + \int_{\Omega} \frac{\gamma(t)}{c(\mathbf{x})^2} |\partial_t u(\mathbf{x}, t)|^2 d\mathbf{x} &\leq \left| \int_{\Omega} c(\mathbf{x})^{-2} G_{\gamma}(\mathbf{x}, t) \partial_t u(\mathbf{x}, t) d\mathbf{x} \right| \\ &\leq \frac{1}{2} \int_{\Omega} \frac{\gamma(t)}{c(\mathbf{x})^2} |\partial_t u(\mathbf{x}, t)|^2 d\mathbf{x} + \frac{1}{2} \int_{\Omega} \frac{1}{\gamma(t)c(\mathbf{x})^2} |G_{\gamma}(\mathbf{x}, t)|^2 d\mathbf{x}. \end{aligned}$$

It can be written as

$$\frac{d}{dt} E_{\text{total},u}(t) \leq \frac{d}{dt} E_{\text{total},u}(t) + \frac{1}{2} \int_{\Omega} \frac{\gamma(t)}{c(\mathbf{x})^2} |\partial_t u(\mathbf{x}, t)|^2 d\mathbf{x} \leq \frac{1}{2} \int_{\Omega} \frac{1}{\gamma(t)c(\mathbf{x})^2} |G_{\gamma}(\mathbf{x}, t)|^2 d\mathbf{x}. \quad (8)$$

For any $t \geq 0$, integrating from 0 to t gives

$$E_{\text{total},u}(t) \leq E_{\text{total},u}(0) + \frac{1}{2} \int_0^t \int_{\Omega} \frac{1}{\gamma(\tau)c(\mathbf{x})^2} |G_{\gamma}(\mathbf{x}, \tau)|^2 d\mathbf{x} d\tau. \quad (9)$$

Lemma 4. *For the solution p of (1) and $g = p|_{\partial\Omega \times [0, \infty)}$ with the assumptions (3), we have*

$$E\partial_t^2 g \in L^2(\Omega \times [0, \infty)) \quad \text{and} \quad E\partial_t g \in L^2(\Omega \times [0, \infty)).$$

By Lemma 4, we have

$$\int_0^{\infty} \int_{\Omega} \frac{1}{\gamma(t)c(\mathbf{x})^2} |G_{\gamma}(\mathbf{x}, t)|^2 d\mathbf{x} dt < \infty, \quad (10)$$

and thus the integral on the right-hand side of (9) is finite. Hence $E_{\text{total},u}(t)$ remains bounded and thus the solution u is global. Again integrating (8) from 0 to T gives

$$E_{\text{total},u}(T) + \frac{1}{2} \int_0^T \int_{\Omega} \frac{\gamma(t)}{c(\mathbf{x})^2} |\partial_t u(\mathbf{x}, t)|^2 d\mathbf{x} dt \leq E_{\text{total},u}(0) + \frac{1}{2} \int_0^T \int_{\Omega} \frac{1}{\gamma(t)c(\mathbf{x})^2} |G_{\gamma}(\mathbf{x}, \tau)|^2 d\mathbf{x} d\tau.$$

and thus

$$\int_0^{\infty} \int_{\Omega} \frac{\gamma(t)}{c(\mathbf{x})^2} |\partial_t u(\mathbf{x}, t)|^2 d\mathbf{x} dt < \infty$$

and thus for a.e. fixed $\mathbf{x} \in \Omega$, $\partial_t u(\mathbf{x}, t) \rightarrow 0$ as $t \rightarrow \infty$.

Now we show that for a.e. $\mathbf{x} \in \Omega$, $u(\mathbf{x}, t) \rightarrow 0$ as $t \rightarrow \infty$. Since $\lim_{t \rightarrow \infty} \partial_t u(\mathbf{x}, t) = 0$, there is a function u_{∞} on \mathbb{R}^n such that $u(\mathbf{x}, t) \rightarrow u_{\infty}(\mathbf{x})$. Then from (4) and $\lim_{t \rightarrow \infty} G_{\gamma}(\mathbf{x}, t) = 0$ (by (10)), we have

$$c(\mathbf{x})\Delta u_{\infty}(\mathbf{x}) = 0 \quad \text{and} \quad u_{\infty}|_{\partial\Omega} = 0.$$

Therefore we have $u_{\infty} = 0$ by strong maximum principle in [17, Chapter 6] and thus

$$\lim_{t \rightarrow \infty} u(\mathbf{x}, t) = 0.$$

The uniqueness of u follows from (9) and the uniqueness of the solution p . □

It remains to prove Lemma 4:

Proof of Lemma 4. Now consider the following energy function: for $D_{\mathbf{x}}^{\alpha} = \partial_{x_1}^{\alpha_1} \partial_{x_2}^{\alpha_2} \cdots \partial_{x_n}^{\alpha_n}$, $\alpha = (\alpha_1, \alpha_2, \dots, \alpha_n) \in \mathbb{N} \cup \{0\}$ and $|\alpha| = \sum_{i=1}^n \alpha_i \leq 1$,

$$E_{\text{total},p}^{\alpha}(t) = \frac{1}{2} \int_{\mathbb{R}^n} (c(\mathbf{x})^{-2} |\partial_t D_{\mathbf{x}}^{\alpha} p(\mathbf{x}, t)|^2 + |\nabla D_{\mathbf{x}}^{\alpha} p(\mathbf{x}, t)|^2) d\mathbf{x} + \int_0^t \int_{\mathbb{R}^n} F_{\alpha}(\mathbf{x}, \tau) D_{\mathbf{x}}^{\alpha} \partial_{\tau} p(\mathbf{x}, \tau) d\mathbf{x} d\tau,$$

where $F_\alpha(\mathbf{x}, t) = [D_{\mathbf{x}}^\alpha, c(\mathbf{x})^{-2}](\partial_t^2 p(\mathbf{x}, t) + \gamma(t)\partial_t p(\mathbf{x}, t))$ and $[A, B] = AB - BA$ is commutator. Differentiating and using the PDE in (1) with Green's Theorem (7) and compactness of p ([3, Chapter 7.4]) yields

$$\frac{d}{dt} E_{\text{total}, p}^\alpha(t) = - \int_{\mathbb{R}^n} \frac{\gamma(t)}{c(\mathbf{x})^2} |\partial_t D_{\mathbf{x}}^\alpha p(\mathbf{x}, t)|^2 d\mathbf{x} \leq 0. \quad (11)$$

Integrating (11) in time gives

$$\int_0^\infty \int_{\mathbb{R}^n} \frac{\gamma(t)}{c(\mathbf{x})^2} |\partial_t D_{\mathbf{x}}^\alpha p(\mathbf{x}, t)|^2 d\mathbf{x} dt \leq 2E_{\text{total}, p}^\alpha(0) < \infty,$$

which implies $\partial_t p \in L^2([0, \infty); H^1(\mathbb{R}^n))$ with assumption (3). By Trace Theorem [17, Chapter 5] and the boundedness of the harmonic extension operator $E : H^s(\partial\Omega) \rightarrow H^{s+\frac{1}{2}}(\Omega)$, we have $\partial_t g \in L^2(\partial\Omega \times [0, \infty))$ and

$$\|E\partial_t g(\cdot, t)\|_{L^2(\Omega)} \leq \|E\partial_t g(\cdot, t)\|_{H^{\frac{1}{2}}(\Omega)} \leq C\|\partial_t g(\cdot, t)\|_{H^0(\partial\Omega)},$$

which implies

$$E\partial_t g \in L^2(\Omega \times [0, \infty)).$$

Similarly, considering the following energy functional

$$\begin{aligned} E_{\text{high}, p}^\alpha(t) &= \frac{1}{2} \int_{\mathbb{R}^n} (c(\mathbf{x})^{-2} |\partial_t^2 D_{\mathbf{x}}^\alpha p(\mathbf{x}, t)|^2 + |\nabla \partial_t D_{\mathbf{x}}^\alpha p(\mathbf{x}, t)|^2) d\mathbf{x} \\ &\quad + \int_0^t \int_{\mathbb{R}^n} \left(\frac{\gamma'(\tau)}{c(\mathbf{x})^2} \partial_\tau D_{\mathbf{x}}^\alpha p(\mathbf{x}, \tau) + \partial_\tau F_\alpha(\mathbf{x}, \tau) \right) \partial_\tau^2 D_{\mathbf{x}}^\alpha p(\mathbf{x}, \tau) d\mathbf{x} d\tau, \end{aligned}$$

we have

$$\frac{d}{dt} E_{\text{high}, p}^\alpha(t) = - \int_{\mathbb{R}^n} \frac{\gamma(t)}{c(\mathbf{x})^2} |\partial_t^2 D_{\mathbf{x}}^\alpha p(\mathbf{x}, t)|^2 d\mathbf{x} \leq 0.$$

Notice that from (1) with assumptions (3), $\partial_t^2 D_{\mathbf{x}}^\alpha p(\mathbf{x}, 0) \in L^2(\mathbb{R}^n)$ and $\partial_t D_{\mathbf{x}}^\alpha p(\mathbf{x}, 0) = 0$ and thus

$$\int_0^\infty \int_{\mathbb{R}^n} \frac{\gamma(t)}{c(\mathbf{x})^2} |\partial_t^2 D_{\mathbf{x}}^\alpha p(\mathbf{x}, t)|^2 d\mathbf{x} dt \leq 2E_{\text{high}, p}^\alpha(0) < \infty.$$

Hence we have $\partial_t^2 p \in L^2([0, \infty); H^1(\mathbb{R}^n))$. Again by Trace Theorem [17, Chapter 5], and the boundedness of the harmonic extension operator, we have

$$E\partial_t^2 g \in L^2(\Omega \times [0, \infty)).$$

□

Now we are ready to prove Theorem 1:

Proof of Theorem 1. Let us consider the solutions \tilde{u}_k of (5) with

$$\lim_{t \rightarrow \infty} \tilde{u}_k(t) = \lim_{t \rightarrow \infty} \tilde{u}'_k(t) = 0 \quad (12)$$

The solution \tilde{u}_k are determined by only $G_{\gamma,k}$ (independent on p_0).

On the other hand, since the Fourier coefficient u_k of the solution u of (4) with initial and boundary values (5) satisfies $u_k, u'_k \rightarrow 0$ as $t \rightarrow \infty$, we have $u_k = \tilde{u}_k$ by uniqueness of ODE solution. Hence p_0 can be uniquely determined from \tilde{u}_k and thus $G_{\gamma,k}$.

By strong maximum principle in [17], Eg is unique and thus we have our assertion. \square

2.1 Constant damping

In the special case where γ is constant, we can derive an explicit inversion procedure.

Theorem 5. *Let $B_{k,\pm} = (-\gamma \pm A_k)/2$ and $A_k = (\gamma^2 - 4\lambda_k^2)^{1/2}$. Then the series $u(\mathbf{x}, t) = \sum_{k \in \mathbb{N}} u_k(t) \psi_k(\mathbf{x})$ converges in $L^2(\Omega, c^{-2})$ and its sum is a solution of (4) with the assumptions (3), where*

$$u_k(t) = A_k^{-1} \int_t^\infty (e^{B_{k,+}(t-\tau)} - e^{B_{k,-}(t-\tau)}) G_{\gamma,k}(\tau) d\tau.$$

Moreover, the initial pressure p_0 can be reconstructed as

$$p_0(\mathbf{x}) = Eg(\mathbf{x}, 0) + \sum_{k \in \mathbb{N}} A_k^{-1} \int_0^\infty (e^{-B_{k,+}\tau} - e^{-B_{k,-}\tau}) G_{\gamma,k}(\tau) d\tau \psi_k(\mathbf{x}).$$

Proof. To check that u_k is a solution of (5), we consider u'_k and u''_k :

$$u'_k(t) = A_k^{-1} \int_t^\infty (B_{k,+} e^{B_{k,+}(t-\tau)} - B_{k,-} e^{B_{k,-}(t-\tau)}) G_{\gamma,k}(\tau) d\tau$$

and

$$u''_k(t) = -G_{\gamma,k}(t) + A_k^{-1} \int_t^\infty (B_{k,+}^2 e^{B_{k,+}(t-\tau)} - B_{k,-}^2 e^{B_{k,-}(t-\tau)}) G_{\gamma,k}(\tau) d\tau.$$

Then using the fact that $(B_{k,\pm})^2 + \gamma B_{k,\pm} + \lambda_k^2 = 0$, we have u_k satisfies (5).

All in all, $u(\mathbf{x}, t) = \sum u_k(t) \psi_k(\mathbf{x})$ satisfies the PDE in (4) with

$$\lim_{t \rightarrow \infty} u_k(t) = \lim_{t \rightarrow \infty} \partial_t u_k(t) = 0 \quad \text{for any } \mathbf{x} \in \Omega, k \in \mathbb{N}.$$

By uniqueness of the solution, we have that u is the solution of (4). \square

We now eliminate the explicit appearance of the extension operator E :

$$\begin{aligned} G_{\gamma,k}(t) &= \int_{\Omega} G_{\gamma}(\mathbf{x}, t) \overline{\psi_k(\mathbf{x})} c(\mathbf{x})^{-2} d\mathbf{x} = \lambda_k^{-2} \int_{\Omega} G_{\gamma}(\mathbf{x}, t) \Delta_{\mathbf{x}} \overline{\psi_k(\mathbf{x})} d\mathbf{x} \\ &= \lambda_k^{-2} \int_{\partial\Omega} (\partial_t^2 g(\mathbf{y}, t) + \gamma(\mathbf{y}) \partial_t g(\mathbf{y}, t)) \partial_{\nu} \overline{\psi_k(\mathbf{y})} ds(\mathbf{y}), \end{aligned}$$

where we used Green's theorem, harmonicity of Eg and $\psi_k = 0$ on $\partial\Omega$, again. Similarly, we have

$$Eg(\mathbf{x}, 0) = \sum_k \lambda_k^{-2} \int_{\partial\Omega} g(\mathbf{y}, 0) \partial_\nu \overline{\psi_k(\mathbf{y})} ds(\mathbf{y}) \psi_k(\mathbf{x}),$$

in $L^2(\Omega, c^{-2})$ sense.

Corollary 6. *Under assumptions (3), the initial function p_0 inside Ω can be reconstructed from the data g in (1) as the following $L^2(\Omega, c^{-2})$ -convergent series:*

$$p_0(\mathbf{x}) = \sum_k \lambda_k^{-2} p_{0,k} \psi_k(\mathbf{x}),$$

where

$$\begin{aligned} p_{0,k} &= \int_{\partial\Omega} g(\mathbf{y}, 0) \partial_\nu \overline{\psi_k(\mathbf{y})} d\mathbf{y} \\ &\quad + A_k^{-1} \int_0^\infty \int_{\partial\Omega} (e^{-B_{k,+}t} - e^{-B_{k,-}t}) (\partial_t^2 g(\mathbf{y}, t) + \gamma(\mathbf{y}) \partial_t g(\mathbf{y}, t)) \partial_\nu \overline{\psi_k(\mathbf{y})} ds(\mathbf{y}) dt, \end{aligned}$$

where $ds(\mathbf{y})$ denotes the surface measure on $\partial\Omega$, again.

3 Numerical inversion procedure

To solve for $p_0(\mathbf{x})$ given observation function $g(\mathbf{x}, t)$ on the observation domain $\partial\Omega$, we consider the following optimization problem:

$$\begin{aligned} \min_{p_0 \in P_{ad}} J(p_0, p) &:= \frac{1}{2} \int_0^T \int_{\partial\Omega} (p(\mathbf{x}, t) - g(\mathbf{x}, t))^2 ds(\mathbf{x}) dt + \frac{\alpha}{2} \int_{\Omega} |p_0(\mathbf{x})|^2 d\mathbf{x} + \beta \int_{\Omega} |p_0(\mathbf{x})| d\mathbf{x} \end{aligned} \quad (13)$$

such that $\partial_t^2 p(\mathbf{x}, t) + \gamma(t) \partial_t p(\mathbf{x}, t) - c(\mathbf{x})^2 \Delta p(\mathbf{x}, t) = 0$, $(\mathbf{x}, t) \in \mathbb{R}^n \times (0, T)$,

$$p(\mathbf{x}, 0) = p_0(\mathbf{x}), \quad \mathbf{x} \in \mathbb{R}^n,$$

$$\partial_t p(\mathbf{x}, 0) = 0, \quad \mathbf{x} \in \mathbb{R}^n,$$

where $p_0 \in P_{ad} = \{L^2(\Omega) : 0 \leq p_l \leq p_0(\mathbf{x}) \leq p_r\}$. Here the first term represents the standard least-squares data fitting term, and the last two terms represent the $L^2 - L^1$ regularization term, with $\alpha, \beta > 0$, that has the ability to reconstruct sparsity patterns in $p_0(\mathbf{x})$.

We first remark that since the functional J is convex with respect to p_0 since the attenuated wave equation is a linear function of p_0 . Thus, there exists a solution pair (p_0^*, p^*) to the minimization problem (13). To characterize the solutions of (13), we use the framework of the Pontryagin's maximum principle (PMP). For this purpose, we formulate the following Hamiltonian function:

$$H(\mathbf{x}, p_0(\mathbf{x}), q(\mathbf{x}, :)) = \frac{\alpha}{2} |p_0(\mathbf{x})|^2 + \beta |p_0(\mathbf{x})| + p_0(\mathbf{x}) [\partial_t q(\mathbf{x}, 0) - \gamma(0) q(\mathbf{x}, 0)], \quad \mathbf{x} \in \Omega, \quad (14)$$

where $q(\mathbf{x}, t)$ solves the following adjoint equation

$$\begin{aligned} \partial_t^2 q(\mathbf{x}, t) - \partial_t[\gamma(t)q(\mathbf{x}, t)] - \Delta[c(\mathbf{x})^2 q(\mathbf{x}, t)] &= -[p(\mathbf{x}, t) - g(\mathbf{x}, t)]\chi_{\partial\Omega}, \quad (\mathbf{x}, t) \in \mathbb{R}^n \times (0, T) \\ q(\mathbf{x}, T) &= 0, \quad \mathbf{x} \in \mathbb{R}^n, \\ \partial_t q(\mathbf{x}, T) &= 0, \quad \mathbf{x} \in \mathbb{R}^n. \end{aligned} \tag{15}$$

We remark that the spatial domain for \mathbf{x} in the definition of H is chosen to be Ω , corresponding to the region of interest. Then, we have the following characterization of the optimal control through the PMP:

Theorem 7. *The optimal initial condition and adjoint (p_0^*, q^*) satisfies the following PMP criterion*

$$H(\mathbf{x}, p_0^*(\mathbf{x}), q^*(\mathbf{x}, :)) = \min_{v \in [p_l, p_r]} H(\mathbf{x}, v, q^*(\mathbf{x}, :)), \quad \forall \mathbf{x} \in \Omega.$$

For the proof of this theorem, we use the standard needle variation technique (see, e.g., [10]). Let $S_\varrho(\mathbf{x}_0)$ be an open ball centered at $\mathbf{x}_0 \in \Omega$ with radius ϱ such that the Lebesgue measure of the ball tends to zero as $\varrho \rightarrow 0$, $\lim_{\varrho \rightarrow 0} |S_\varrho(\mathbf{x}_0)| = 0$. We define the needle variation at \mathbf{x}_0 of $p_0 \in P_{ad}$ as follows:

$$p_0^\varrho(\mathbf{x}) := \begin{cases} p_0(\mathbf{x}) & \text{on } \Omega \setminus S_\varrho(\mathbf{x}_0) \\ w & \text{in } S_\varrho(\mathbf{x}_0) \cap \Omega \end{cases} \tag{16}$$

where $w \in [p_l, p_r]$. We note that $p_0^\varrho \in P_{ad}$ for all $\mathbf{x}_0 \in \Omega$, and for any given $p_0 \in P_{ad}$ (see [10]).

Since $p_0(\mathbf{x}) \in L^\infty(\Omega)$, almost every where in Ω is a Lebesgue point of $p_0(\mathbf{x})$. Therefore, it holds:

$$\|p_0^\varrho - p_0\|_{L^2(\Omega)} = \left(\int_{S_\varrho(\mathbf{x}_0)} |w - p_0(\mathbf{x})|^2 d\mathbf{x} \right)^{\frac{1}{2}} \rightarrow 0, \quad \text{as } \varrho \rightarrow 0, \tag{17}$$

for almost all $\mathbf{x}_0 \in \Omega$. From this fact and the stability result for the attenuated wave equation, we have:

$$\|p_\varrho - p\|_{L^\infty(0, T; L^2(\Omega))} \rightarrow 0, \quad \|q_\varrho - q\|_{L^\infty(0, T; L^2(\Omega))} \rightarrow 0, \quad \|\partial_t q_\varrho - \partial_t q\|_{L^\infty(0, T; L^2(\Omega))} \rightarrow 0, \tag{18}$$

and

$$\|\partial_t p_\varrho(\cdot, 0) - \partial_t p(\cdot, 0)\|_{L^2(\Omega)} \rightarrow 0, \quad \|p_\varrho(\cdot, 0) - p(\cdot, 0)\|_{L^2(\Omega)} \rightarrow 0, \tag{19}$$

where p_ϱ and q_ϱ denote the state and adjoint variables corresponding to p_0^ϱ .

Let p_0 be a minimizer. We then compute the difference of cost functionals to obtain

$$\begin{aligned} J(p_0^\varrho, p_\varrho) - J(p_0, p) &= \int_0^T \int_{\partial\Omega} \left(\frac{p_\varrho(\mathbf{y}, t) + p(\mathbf{y}, t)}{2} - g(\mathbf{y}, t) \right) (p_\varrho(\mathbf{y}, t) - p(\mathbf{y}, t)) ds(\mathbf{y}) dt \\ &\quad + \int_{\Omega} (G(p_0^\varrho(\mathbf{x})) - G(p_0(\mathbf{x}))) d\mathbf{x}, \end{aligned} \tag{20}$$

where $G(p_0) = \frac{\alpha}{2} \int_{\Omega} |p_0(\mathbf{x})|^2 \, d\mathbf{x} + \beta \int_{\Omega} |p_0(\mathbf{x})| \, d\mathbf{x}$. We now introduce an intermediate adjoint problem as follows:

$$\begin{aligned} \partial_t^2 q_{\varrho}(\mathbf{x}, t) - \partial_t[\gamma(t)q_{\varrho}(\mathbf{x}, t)] - \Delta[c(\mathbf{x})^2 q_{\varrho}(\mathbf{x}, t)] &= - \left[\frac{p_{\varrho}(\mathbf{x}, t) + p(\mathbf{x}, t)}{2} - g(\mathbf{x}, t) \right] \chi_{\partial\Omega}, \\ &(\mathbf{x}, t) \in \mathbb{R}^n \times (0, T), \quad (21) \\ q_{\varrho}(\mathbf{x}, T) &= 0, \quad \mathbf{x} \in \mathbb{R}^n, \\ \partial_t q_{\varrho}(\mathbf{x}, T) &= 0, \quad \mathbf{x} \in \mathbb{R}^n. \end{aligned}$$

Standard regularity estimates of (21) gives us the following results:

$$q_{\varrho} \in L^{\infty}(0, T; L^2(\Omega)), \quad \partial_t q_{\varrho} \in L^{\infty}(0, T; L^2(\Omega)) \cap L^2(0, T; L^2(\Omega)). \quad (22)$$

We can state the following lemma related to the difference in the value of the functional J at the needle variation:

Lemma 8. *The following equation holds*

$$J(p_0^{\varrho}, p_{\varrho}) - J(p_0, p) = - \int_{\Omega} (H(\mathbf{x}, p_0^{\varrho}, q_{\varrho}) - H(\mathbf{x}, p_0, q_{\varrho})) \, d\mathbf{x},$$

where H is given as in (14).

Proof. Using (21) in (20), to replace $\left(\frac{p_{\varrho}(\mathbf{x}, t) + p(\mathbf{x}, t)}{2} - g(\mathbf{x}, t)\right)$ with the corresponding left-hand side of the intermediate adjoint problem, integration by parts and the use of the boundary and initial and terminal conditions give the desired result. \square

Now, we can consider the needle variation in the limit $\varrho \rightarrow 0$. We have

Lemma 9. *Let $p_0^* \in P_{ad}$ be a minimizer and $w \in [p_l, p_r]$. Furthermore, let p_0^{ϱ} be defined as in (16), and p_{ϱ} be the solution to the attenuated wave equation (4) with $p_0 = p_0^{\varrho}$. Then, the following holds*

$$0 \leq \lim_{\varrho \rightarrow 0} \frac{1}{|S_{\varrho}(\mathbf{x}_0)|} (J(p_0^{\varrho}, p_{\varrho}) - J(p_0^*, p^*)) = H(\mathbf{x}_0, p_0^*, q^*) - H(\mathbf{x}_0, w, q^*),$$

for almost all $\mathbf{x}_0 \in \Omega$ and $w \in [p_l, p_r]$.

Proof. For any $k \in \mathbb{N}$, we have

$$\begin{aligned} 0 &\leq \frac{1}{|S_{\varrho}(\mathbf{x}_0)|} (J(p_0^{\varrho}, p_{\varrho}) - J(p_0^*, p^*)) \\ &= \frac{1}{|S_{\varrho}(\mathbf{x}_0)|} \int_{\Omega} (H(\mathbf{x}, p_0^{\varrho}, q_{\varrho}) - H(\mathbf{x}, p_0^{\varrho}, q_{\varrho})) \, d\mathbf{x} \\ &= \frac{1}{|S_{\varrho}(\mathbf{x}_0)|} \int_{S_{\varrho}(\mathbf{x}_0)} (H(\mathbf{x}, p_0^*, q^*) - H(\mathbf{x}, w, q^*)) \, d\mathbf{x} \\ &\quad + \frac{1}{|S_{\varrho}(\mathbf{x}_0)|} \int_{S_{\varrho}(\mathbf{x}_0)} \left((p_0^* - w)[(\partial_t q_{\varrho}(\mathbf{x}, 0) - \partial_t q^*(\mathbf{x}, 0)) - \gamma(0)(q_{\varrho}(\mathbf{x}, 0) - q^*(\mathbf{x}, 0))] \right) \, d\mathbf{x}. \end{aligned}$$

Since, $\mathbf{x} \in \Omega \mapsto \left(H(\mathbf{x}, p_0^*, q^*) - H(\mathbf{x}, w, q^*) \right) \in L^1(\Omega)$, convergence results for p_0^ϱ , p_ϱ , and q_ϱ in (17) and (18), we have the following using the mean value theorem:

$$0 \leq \lim_{\varrho \rightarrow 0} \frac{1}{|S_\varrho(\mathbf{x}_0)|} (J(p_0^\varrho, p_\varrho) - J(p_0^*, p^*)) = H(\mathbf{x}_0, p_0^*, q^*) - H(\mathbf{x}_0, w, q^*).$$

□

As a consequence of Lemma 9, we have proved the PMP Theorem 7.

A major advantage of the PMP framework is that the PMP characterization does not involve derivatives of the objective functional J with respect to p_0 , unlike the standard first order optimality conditions using the Euler-Lagrange framework. This motivates the construction of the sequential quadratic Hamiltonian method (SQH) to implement the PMP condition as stated in Theorem 7. The SQH method, developed in its recent form in [10] represents a recent development in the field of successive approximations (SA) schemes. The working principle of these methods is the iterative pointwise minimisation of the Hamiltonian function of the given minimization problem. The starting point of the SQH method is the augmented Hamiltonian function, which is defined as:

$$H_\epsilon(\mathbf{x}, p_0, \tilde{p}_0, q) = H(\mathbf{x}, p_0, q) + \epsilon(p_0 - \tilde{p}_0)^2,$$

where $\epsilon > 0$ is a penalization parameter that is adaptively adjusted at each iteration of the SQH process. Specifically, ϵ is increased if a sufficient decrease in the functional J is not observed, and decreased if J decreases adequately. Here, \tilde{p}_0 represents the previous approximations of the initial condition p_0 , respectively. The purpose of the quadratic term $\epsilon(p_0 - \tilde{p}_0)^2$ is to ensure that the pointwise minimizer of H_ϵ , and thus the updates to p_0 remain close to the prior values \tilde{p}_0 , especially when ϵ is large. It is important to note that during each optimization step, specifically during a minimization sweep over all spatial grid points \mathbf{x} , the values of p and q used are those obtained from the previous iteration. The SQH algorithm is outlined in the following algorithm:

Algorithm 10 (SQH method).

- *Input: initial approx. p_0^0 , max. number of iterations k_{max} , tolerance $\kappa > 0$, $\epsilon > 0$, $\lambda > 1$, $\eta > 0$, and $\zeta \in (0, 1)$; set $\tau > \kappa$, $k := 0$.*
- *Compute the solution p^0 to the damped wave equation given in (13) with initial condition $p_0 = p_0^0$.*
- *While ($k < k_{max}$ && $\tau > \kappa$) do*
 - (a) Compute the solution q^k to the adjoint problem (15) with $p = p^k$.*
 - (b) Determine p_0^{k+1} such that the following optimization problem is satisfied*

$$H_\epsilon(\mathbf{x}, p_0^{k+1}, p_0^k, q^k) = \min_{v \in [p_l, p_r]} H_\epsilon(\mathbf{x}, v, p_0^k, q^k),$$

at almost all $\mathbf{x} \in \Omega$.

- (c) Compute the solution p^{k+1} to the damped wave equation given in (13) with initial condition $p_0 = p_0^{k+1}$*
- (d) Compute $\tau := \|p_0^{k+1} - p_0^k\|_{L^2(\Omega)}^2$.*

- (e) If $J(p_0^{k+1}, p^{k+1}) - J(p_0^k, p^k) > -\eta\tau$, then increase ϵ with $\epsilon = \lambda\epsilon$ and go to Step (b).
 Else if $J(p_0^{k+1}, p^{k+1}) - J(p_0^k, p^k) \leq -\eta\tau$, then decrease ϵ with $\epsilon = \zeta\epsilon$ and continue.
 (f) Set $k := k + 1$.

• end While

In Step (e) of this algorithm, if the inequality $J(p_0^{k+1}, p^{k+1}) - J(p_0^k, p^k) > -\eta\tau$ holds, it indicates that a sufficient decrease in the objective functional J has not been achieved. In such a case, ϵ is increased (since $\lambda > 1$), and the optimization in Step (b) is repeated with the updated augmented Hamiltonian function. In contrast, if the inequality does not hold, it confirms that the required reduction in J has been achieved. The updated initial condition p_0^{k+1} is then adopted, together with the corresponding updates p^{k+1} and q^{k+1} for the damped wave equation and its adjoint. In this situation, ϵ is reduced by a factor $\zeta < 1$.

Theorem 11. Let (p_0^k, p^k) and (p_0^{k+1}, p^{k+1}) be generated by the SQH method (Algorithm 10) applied to (13), with $p_0^{k+1}, p^k \in P_{ad}$. Then, there exists a constant $C > 0$, independent of ϵ and p_0^k , such that for the current value of $\epsilon > 0$ chosen by Algorithm 10, the following inequality holds:

$$J(p_0^{k+1}, p^{k+1}) - J(p_0^k, p^k) \leq -(\epsilon - C) \|p_0^{k+1} - p_0^k\|_{L^2(\Omega)}^2. \quad (23)$$

In particular, this implies $J(p_0^{k+1}, p^{k+1}) - J(p_0^k, p^k) \leq -\eta\tau$ for $\epsilon \geq C + \eta$ and $\tau = \|p_0^{k+1} - p_0^k\|_{L^2(\Omega)}^2$.

Proof. We have the following Hamiltonian function

$$H(\mathbf{x}, p_0(\mathbf{x}), q(\mathbf{x})) = \frac{\alpha}{2}|p_0(\mathbf{x})|^2 + \beta|p_0(\mathbf{x})| + p_0(\mathbf{x})[\partial_t q(\mathbf{x}, 0) - \gamma(0)q(\mathbf{x}, 0)].$$

In Step (b) of Algorithm 10, we have that for almost all $\mathbf{x} \in \Omega$ it holds:

$$H_\epsilon(\mathbf{x}, p_0^{k+1}, p_0^k, q^k) \leq H_\epsilon(\mathbf{x}, v, p_0^k, q^k),$$

for all $v \in [p_l, p_r]$. Therefore, we have

$$H_\epsilon(\mathbf{x}, p_0^{k+1}, p_0^k, q^k) \leq H_\epsilon(\mathbf{x}, p_0^k, p_0^k, q^k) = H(\mathbf{x}, p_0^k, q^k).$$

Hence, we obtain the inequality

$$H(\mathbf{x}, p_0^{k+1}, q^k) + \epsilon|p_0^{k+1} - p_0^k|^2 \leq H(\mathbf{x}, p_0^k, q^k). \quad (24)$$

Define $\delta p = p^{k+1} - p^k$, $l(p_0) = \frac{\alpha}{2}|p_0|^2 + \beta|p_0|$ and $\delta p_0 = p_0^{k+1} - p_0^k$. We have

$$\begin{aligned}
& J(p_0^{k+1}, p^{k+1}) - J(p_0^k, p^k) \\
&= \frac{1}{2} \int_0^T \int_{\partial\Omega} 2(p^k(\mathbf{y}, t) - g(\mathbf{y}, t))\delta p(\mathbf{y}, t) + (\delta p(\mathbf{y}, t))^2 \, ds(\mathbf{y})dt + \int_{\Omega} l(p_0^{k+1})(\mathbf{x}) - l(p_0^k)(\mathbf{x}) \, d\mathbf{x} \\
&= \frac{1}{2} \int_0^T \int_{\partial\Omega} (\delta p(\mathbf{y}, t))^2 \, ds(\mathbf{y})dt + \int_0^T \int_{\partial\Omega} (p^k(\mathbf{y}, t) - g(\mathbf{y}, t))\delta p(\mathbf{y}, t) \, ds(\mathbf{y})dt \\
&\quad + \int_{\Omega} l(p_0^{k+1})(\mathbf{x}) - l(p_0^k)(\mathbf{x}) \, d\mathbf{x} \\
&= \frac{1}{2} \int_0^T \int_{\partial\Omega} (\delta p(\mathbf{y}, t))^2 \, ds(\mathbf{y})dt + \int_{\Omega} [\partial_t q^k(\mathbf{x}, 0) - \gamma(0)q^k(\mathbf{x}, 0)]\delta p_0(\mathbf{x}) \, d\mathbf{x} \\
&\quad + \int_{\Omega} l(p_0^{k+1})(\mathbf{x}) - l(p_0^k)(\mathbf{x}) \, d\mathbf{x} \\
&= \frac{1}{2} \int_0^T \int_{\partial\Omega} (\delta p(\mathbf{y}, t))^2 \, ds(\mathbf{y})dt + \int_{\Omega} H(\mathbf{x}, p_0^{k+1}, q^k) - H(\mathbf{x}, p_0^k, q^k) \, d\mathbf{x} \\
&\leq C \|p_0^{k+1} - p_0^k\|_{L^2(\Omega)}^2 - \epsilon \|p_0^{k+1} - p_0^k\|_{L^2(\Omega)}^2,
\end{aligned}$$

where the last step follows from the equation following (24) and the standard stability estimate of solutions of (4). \square

This theorem shows that, if (p_0^k, p^k) are not already optimal, it is possible to choose $\epsilon > C$ to obtain a successful minimization step. We have the following corollary as a consequence of Theorem 11.

Corollary 12. *The sequence $\{\epsilon\}$ of the SQH iterates is bounded.*

Proof. From Algorithm 10, we note that the successful k -th minimization step is performed with $\epsilon = (C + \eta)$, where C is estimated in Theorem 11 above. Then, there is a constant $\bar{\epsilon}$ related to the stability estimate of the attenuated wave equation (4), the data of the problem, and the regularization and SQH parameters, that provides an upper bound $\epsilon \leq \bar{\epsilon}$ of the sequence $\{\epsilon\}$ of the SQH iterates. \square

This corollary ensures that the SQH algorithm converges, which is what we prove in the next theorem.

Theorem 13. *Under the assumptions of Theorem 11, if in Algorithm 10, at every k -th iterate, $\epsilon = C + \eta$ is chosen (and tolerance $\kappa = 0$, so that the algorithm never stops), then the following holds*

1. $\lim_{k \rightarrow \infty} |J(p_0^{k+1}, p^{k+1}) - J(p_0^k, p^k)| = 0$
2. $\lim_{k \rightarrow \infty} \|p_0^{k+1} - p_0^k\|_{L^2(\Omega)} = 0.$

Proof. The first statement follows from (23), since ϵ can be chosen greater than C , which would imply that the sequence $\{J(p_0^k, p^k)\}$ is monotonically decreasing the \mathbb{R} and is a Cauchy sequence, hence convergent. To prove 2, we rewrite (23) as follows

$$\|p_0^{k+1} - p_0^k\|_{L^2(\Omega)}^2 \leq \frac{1}{\eta} \left[J(p_0^k, p^k) - J(p_0^{k+1}, p^{k+1}) \right].$$

Therefore we have the partial sum

$$\sum_{k=0}^K \|p_0^{k+1} - p_0^k\|_{L^2(\Omega)}^2 \leq \frac{1}{\eta} \left[J(p_0^0, p^0) - J(p_0^{K+1}, p^{K+1}) \right].$$

This shows that in the limit $K \rightarrow \infty$, the series with positive elements $\|p_0^{k+1} - p_0^k\|_{L^2(\Omega)}^2$ is convergent, which proves the result. \square

Theorem 13 guarantees that Algorithm 10 is well defined for $\kappa > 0$. Hence, there is an iteration number $k_0 \in \mathbb{N}$ such that $\|p_0^{k_0+1} - p_0^{k_0}\|_{L^2(\Omega)} \leq \kappa$. This implies that the SQH algorithm stops in finitely many steps.

3.1 CNN-guided initial guess construction

To solve for p_0 using the SQH scheme, we construct the initial guess, using a CNN algorithm. The architecture of the CNN is given as follows: The CNN begins with an input convolutional layer consisting of 32 filters with a kernel size of 3 and a stride of 2, using the ReLU activation function. A MaxPooling layer with a pooling size of 2 is applied immediately afterward. Max pooling reduces the temporal resolution of the feature maps by retaining only the maximum value within each non-overlapping window of size 2, thereby providing a form of translational invariance and mitigating overfitting by discarding less relevant activations. The network then incorporates three additional convolutional layers, each employing 64 filters, a kernel size of 3, and a stride of 2, with ReLU activation. The first two of these layers are each followed by a MaxPooling layer (with pool size 2), further downsampling the feature representation and emphasizing the most salient local features. After the final convolutional stage, the output tensor is flattened into a one-dimensional vector. This vector is passed through four fully connected dense layers, each containing 64 neurons activated by ReLU, enabling the extraction of increasingly abstract nonlinear feature relationships. The architecture concludes with a dense output layer employing a linear activation function.

The output of the CNN and the output of the time-reversal are summed up to provide the initial guess for the SQH algorithm.

4 Numerical results

In this section, we present the results of our SQH method to solve the inverse problem to obtain the initial damped wave acoustic pressure p_0 from observational data. We first present the results in a one-dimensional setup. For this purpose, we choose our domain $\Omega = (-1, 1)$ and the final time of observations as $T = 1$. The complete observation domain $\partial\Omega = \{x = -1, 1\}$. We choose a non-trapping sound speed $c(x) = 1 + w(x) * 0.1 * \cos(2\pi x)$, where $w(x)$ is a mollifier centered at the middle of the domain with radius $\sqrt{0.5}$, achieving a maximum value of 1. The damping coefficient $\gamma(t)$ is chosen as $\exp(-t)$. For the

spatial grid, we choose 200 points, whereas our time grid comprises of 200 points. To generate the data, we solve the wave equation (4) in free space on a spatial grid with 50 points and on the temporal grid at 50 time points, and then interpolate the solution on the original grid to collect the data on the boundary points $x = -1, 1$. The choice of the regularization weights are $\alpha \in [0.1, 0.4]$ and $\beta \in [0.001, 0.01]$. We then add 10% additive Gaussian noise to the data.

For training the CNN, we generated a dataset of 750 samples: For the first 150 samples, the output was chosen as Gaussian functions with centers randomly drawn from the interval $(-0.5, 0.1) \cup (0.3, 0.7)$ and widths drawn from $(50, 70) \cup (120, 150)$. For the next 350 samples, the output was chosen as characteristic functions with centers in the interval $(-0.7, -0.1)$ and widths in the interval $(0.1, 0.7)$. For the last 250 samples, we have a sum of a Gaussian and characteristic function as output, with centers of the Gaussian drawn from the interval $(-0.9, 0.9)$ and widths in $(50, 150)$ while the centers of the characteristic function are in $(-0.9, 0.9)$ and widths in $(0.1, 0.3)$. The number of epochs chosen for the training was 500, with batch size 32. The optimizer was chosen as ‘‘Adam’’ with the Huber loss function. The Huber loss offers a balance between the commonly used Mean Square Error (MSE) and Mean Absolute Error (MAE), since it is quadratic for small errors and linear for large errors, making it robust to outliers while still allowing for accurate fits. Unlike MAE, it is smooth and differentiable everywhere, which leads to more stable and efficient optimization. Overall, it provides better gradient behavior and improved performance on noisy data compared to MSE or MAE alone.

We compare our reconstructions with the time-reversal method, obtained by solving the wave equation (4) backwards in time with boundary condition as the observation data, and the reconstructions obtained using our CNN. The time-reversal solution at the final time gives an approximation to the initial condition to the original wave equation (4). For qualitative comparison, we also use the quantitative figure of merits: Mean Square Error (MSE), the Peak Signal-to-Noise Ratio (PSNR), and the Structural Similarity Index Measure (SSIM) as defined below:

$$MSE(I^1, I^2) = \frac{1}{n} \sum_{p=1}^n (I_p^1 - I_p^2)^2, \quad PSNR(I^1, I^2) = 10 \log_{10} \left(\frac{[\max(I^1, I^2)]^2}{MSE(I^1, I^2)} \right),$$

where p represents a pixel and n is the total number of pixels, and

$$SSIM(I^1, I^2) = \frac{(2\mu_{I^1}\mu_{I^2} + C_1)(2\sigma_{I^1 I^2} + C_2)}{(\mu_{I^1}^2 + \mu_{I^2}^2 + C_1)(\sigma_{I^1}^2 + \sigma_{I^2}^2 + C_2)},$$

where μ_{I^1} and μ_{I^2} denote the average intensities of the images I^1 and I^2 , respectively, $\sigma_{I^1}^2$ and $\sigma_{I^2}^2$ represent the corresponding intensity variances, and $\sigma_{I^1 I^2}$ is the covariance between the two images. IMMSE quantifies the average squared pixel-wise difference between two images and is purely error-based, without considering human visual perception. PSNR is a logarithmic transformation of MSE that expresses the fidelity of a reconstructed image relative to the maximum possible pixel intensity; higher PSNR indicates lower error, but it still does not account for structural content. SSIM, on the other hand, compares images based on luminance, contrast, and structural information, making it more aligned with human visual perception. Thus, IMMSE and PSNR focus on pixel-wise accuracy, while SSIM evaluates perceptual similarity.

For the first test case, we choose the true p_0 to be a Gaussian centered at $x = 0.5$ with a peak value of 1.0 and standard deviation 0.25. The reconstructions are given in Figure 1.

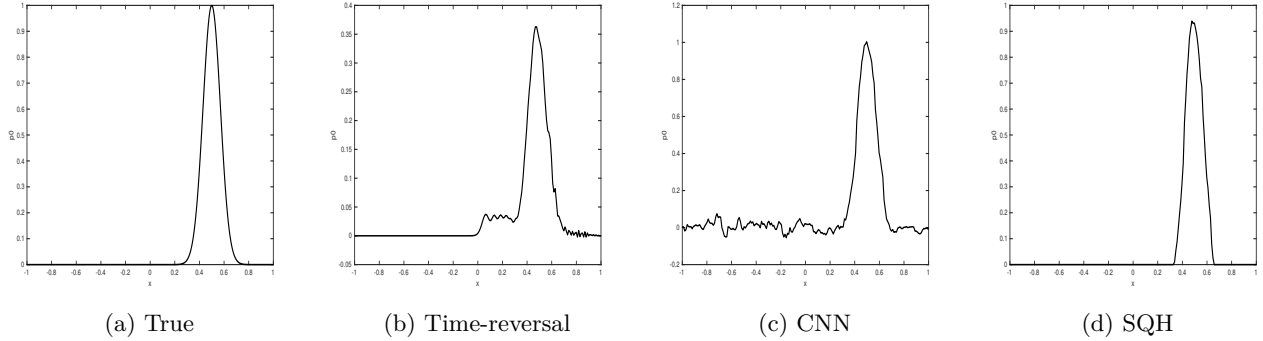


Figure 1: Test Case 1: Reconstructions in 1D with the Gaussian phantom

We observe that the time-reversal solution has significant loss of contrast due to damping and also has poor resolution. The reconstructions obtained using the CNN, improve the peak contrast significantly, but has poor background contrast. On the other hand, the reconstructions obtained using the SQH method have superior contrast and resolution. We note that the peak and the sparsity patterns in the reconstructions are well captured due to the presence of the L^1 regularization term.

For the second test case, we choose the true p_0 to be a characteristic function centered at $x = -0.2$ with a value of 1.0 and width 0.3. The reconstructions are given in Figure 2.

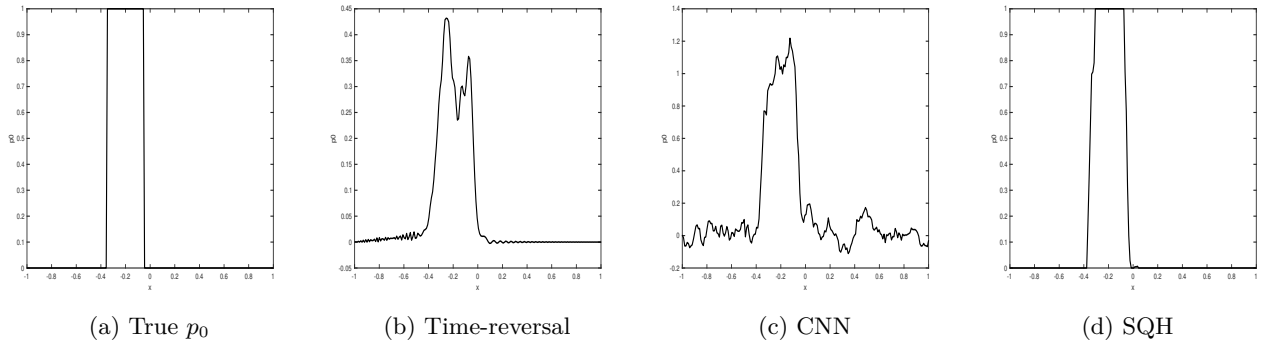


Figure 2: Test Case 2: Reconstructions in 1D with the characteristic phantom

We now observe significant loss of contrast and resolution with the time-reversal reconstruction, with a dip along the place of the sharp-edge. With the CNN, the contrast improves again, but there seems to be appearance of spurious peaks, coupled with poor background contrast. On the other hand, with the SQH algorithm, we obtain a sharp-edge reconstruction, with a perfect background, demonstrating the superiority of our proposed method.

For the third test case, we choose the true p_0 to be a combination of a Gaussian centered at $x = 0.5$ with a peak value of 0.5 and standard deviation 0.25 and a characteristic function centered at $x = -0.2$ with a value of 1.0 and width 0.2. The reconstructions are shown in Figure 3.

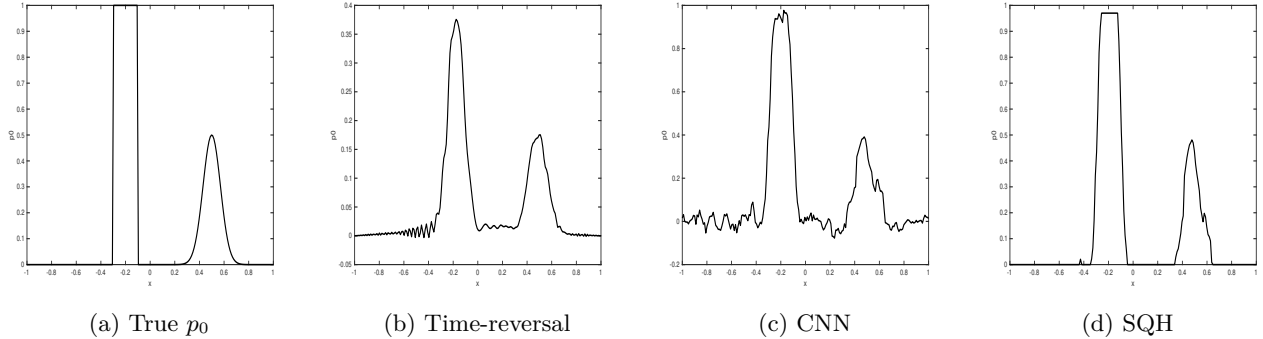


Figure 3: Test Case 3: Reconstructions in 1D with the mixed phantom

We again observe the poor reconstruction quality with the time-reversal algorithm, which improves in contrast with the CNN but still has poor background reconstruction. With the SQH, we again obtain the sharp-edge and sparsity patterns in the background, resulting in high resolution and contrast reconstruction.

We now proceed to reconstructions in a two dimensional setup, where we choose our domain $\Omega = (-1, 1) \times (-1, 1)$, the observation boundary as $\partial\Omega$, and the final time of observation as $T = 2$. We choose a non-trapping sound speed $c(\mathbf{x}) = 1 + w(\mathbf{x}) * [0.1 * \cos(2\pi x_1) + 0.05 * \sin(2\pi x_2)]$, where $w(\mathbf{x})$ is a mollifier centered at the middle of the domain with radius $\sqrt{0.5}$, with a maximum value of 1. For the spatial grid, we choose 100 points along each dimension, whereas our time grid comprises of 200 points. To generate the data, we solve the wave equation (4) in free space on a spatial grid with 50 points and on the temporal grid at 50 time points, and then interpolate the solution on the original grid to collect the data on the boundary $\partial\Omega$.

For training the CNN, we generated a dataset of 750 samples: For the first 150 samples, the output was chosen as Gaussian functions with centers randomly drawn from the interval $(-0.9, 0.9)$ and widths drawn from $(50, 150)$. For the next 350 samples, the output was chosen as characteristic functions with centers in the interval $(-0.9, 0.9)$ and widths in the interval $(0.1, 0.5)$. For the last 250 samples, we have a sum of a Gaussian and characteristic function as output, with centers of the Gaussian drawn from the interval $(-0.9, 0.9)$ and widths in $(10, 60)$ while the centers of the characteristic function are in $(-0.9, 0.9)$ and widths in $(0.1, 0.5)$. The number of epochs chosen for the training was 500, with batch size 32. The optimizer was chosen as “Adam” with the Huber loss function.

In the next test case, our true phantom is a Gaussian phantom with center at $(-0.3, -0.3)$ and standard deviation 0.5. The reconstructions are shown in Figure 4.

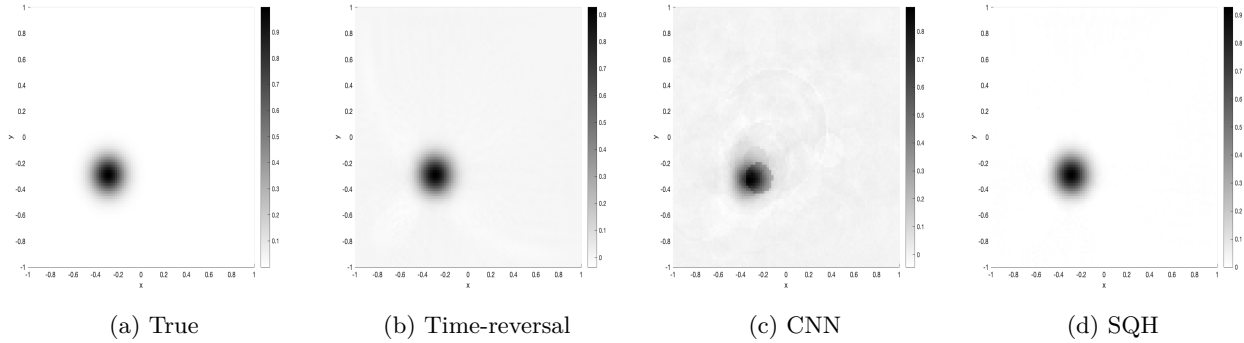


Figure 4: Test Case 4: Reconstructions in 2D with a Gaussian phantom

We observe that the time-reversal algorithm provides good resolution but not the best contrast. The CNN reconstruction is not the best in terms of resolution. On the other hand, the SQH algorithm provides superior resolution and contrast, outperforming both the methods.

For the fifth test case, we now consider a disk phantom centered at $(-0.2, -0.2)$ with radius 0.1. The reconstructions are shown in Figure 5.

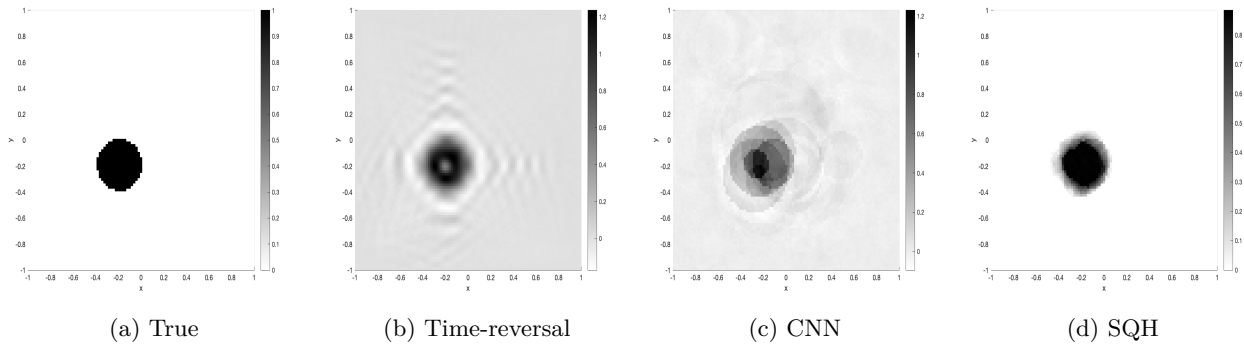


Figure 5: Test Case 5: Reconstructions in 2D with a disk phantom

We now notice the presence of severe artifacts in the reconstruction with the time-reversal algorithm, leading to poor resolution and contrast. The CNN reconstruction does capture the disk discontinuity with a better contrast, but has other superficial structures present. The SQH algorithm is able to significantly clear off the artifacts due to the sparsity promoting feature and the contrast and resolution are far more better.

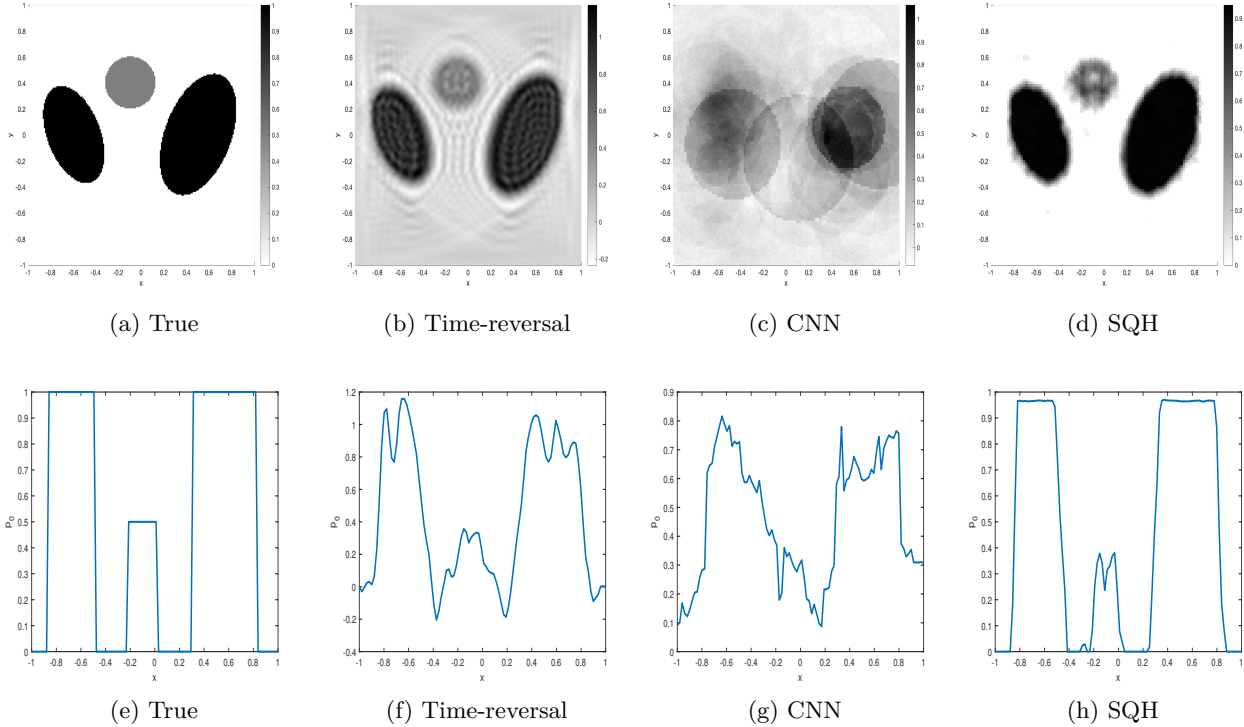


Figure 6: Test Case 6: Reconstructions in 2D with the heart and lung phantom; Top row corresponds to the 2D profiles; Bottom row corresponds to a 1D cross sectional profile

For the final test case, we consider a heart and lung phantom, represented by 2 ellipses and a disk. The reconstructions, with both 2D and cross-sectional 1D views, are shown in Figure 6. We again notice the presence of significant artifacts in the time-reversal reconstruction, leading to poor contrast and resolution. The CNN is expected to give a poor reconstruction with lot of superficial structures, since it was only trained on disks and Gaussians and at the most two objects, instead of ellipses and combination of three objects. However, some sharp edges in the CNN reconstruction help with the initial guess of the SQH algorithm, which now significantly improves the contrast and resolution significantly. This is also noted in the cross-sectional views of the reconstruction.

We now list the MSE, PSNR, and SSIM values of the reconstructions in Tables 1, 2, and 3.

Phantom	Test Case	TR	CNN	SQH
1D Gaussian	Test case 1	2.5e-2	8e-4	5e-4
1D Characteristic function	Test case 2	7.2e-2	1e-2	4e-3
1D Mixed	Test case 3	6.1e-2	9.8e-2	7.3e-3
2D Gaussian	Test case 4	4.5e-5	6.4e-4	2.9e-5
2D Disk	Test case 5	4.3e-3	8.4e-3	3.8e-3
2D Heart-Lung	Test case 6	1.8e-2	7e-2	1.1e-2

Table 1: MSE values for the various test cases.

Phantom	Test Case	TR	CNN	SQH
1D Gaussian	Test case 1	15.94	31.22	32.74
1D Characteristic function	Test case 2	11.46	19.94	23.71
1D Mixed	Test case 3	12.13	20.10	21.34
2D Gaussian	Test case 4	43.43	31.92	45.30
2D Disk	Test case 5	23.64	20.78	24.14
2D Heart-Lung	Test case 6	17.41	11.55	19.55

Table 2: PSNR values for the various test cases.

Phantom	Test Case	TR	CNN	SQH
1D Gaussian	Test case 1	0.77	0.47	0.94
1D Characteristic function	Test case 2	0.71	0.2	0.92
1D Mixed	Test case 3	0.59	0.35	0.95
2D Gaussian	Test case 4	0.89	0.76	0.96
2D Disk	Test case 5	0.66	0.47	0.97
2D Heart-Lung	Test case 6	0.28	0.13	0.84

Table 3: SSIM values for the various test cases.

We observe that the TR method gives high values of MSE and low values of PSNR. The MSE decreases and PSNR increases with the CNN but is significantly outperformed by the SQH algorithm. The striking feature is the SSIM values of the SQH algorithm which is close to 1 for all the test cases compared to the other two methods, further demonstrating the robustness and versatility of our proposed reconstruction framework.

5 Conclusions

We have presented a theoretical framework for the recovery of the initial pressure of the attenuated wave equation from the boundary datum, using the idea of harmonic extension. When the damping is constant, we also obtained an explicit reconstruction formula for the initial pressure, given by a series representation. Furthermore, we present a gradient free optimization framework, in the realm of the Pontryagin’s maximum principle, and develop the SQH method, guided by initial guess generated using a CNN, to provide superior reconstructions. Numerical experiments in one and two dimensions demonstrate the robustness and accuracy of our framework.

Acknowledgment

S. Moon thanks The University of Texas at Arlington for its hospitality during 2025 when most of the presented work was done.

References

- [1] B. J. Adesokan, K. Knudsen, V. P. Krishnan, and S. Roy. A fully non-linear optimization approach to acousto-electric tomography. *Inverse problems*, 34(10):104004, 2018.
- [2] M. Agranovsky and P. Kuchment. Uniqueness of reconstruction and an inversion procedure for thermoacoustic and photoacoustic tomography with variable sound speed. *Inverse Problems*, 23(5):2089, 2007.
- [3] S. Alinhac. *Hyperbolic partial differential equations*. Springer Science & Business Media, 2009.
- [4] H. Ammari, E. Bossy, J. Garnier, L. Nguyen, and L. Seppecher. A reconstruction algorithm for ultrasound-modulated diffuse optical tomography. *Proceedings of the American Mathematical Society*, 142(9):3221–3236, 2014.
- [5] H. Ammari, E. Bossy, V. Jugnon, and H. Kang. Mathematical modeling in photoacoustic imaging of small absorbers. *SIAM Review*, 52(4):677–695, 2010.
- [6] Habib Ammari, Elie Bretin, Vincent Jugnon, and Abdul Wahab. Photoacoustic imaging for attenuating acoustic media. In *Mathematical modeling in biomedical imaging II: optical, ultrasound, and opto-acoustic tomographies*, pages 57–84. Springer, 2012.
- [7] M. A. Anastasio, J. Zhang, D. Modgil, and P. J. La Rivière. Application of inverse source concepts to photoacoustic tomography. *Inverse Problems*, 23(6):S21, 2007.
- [8] J. Bartsch, A. Borzì, F. Fanelli, and S. Roy. A numerical investigation of brockett’s ensemble optimal control problems. *Numerische Mathematik*, 149(1):1–42, 2021.
- [9] A.G. Bell. On the production and reproduction of sound by light. *American Journal of Science*, 20:305–324, October 1880.
- [10] A. Borzì. *The Sequential Quadratic Hamiltonian Method: Solving Optimal Control Problems*. Chapman and Hall/CRC Numerical Analysis and Scientific Computing Series. Taylor & Francis, 2023.
- [11] T. Breitenbach and A. Borzì. On the SQH scheme to solve nonsmooth pde optimal control problems. *Numerical Functional Analysis and Optimization*, 40(13):1489–1531, 2019.
- [12] T. Breitenbach and A. Borzì. A sequential quadratic hamiltonian method for solving parabolic optimal control problems with discontinuous cost functionals. *Journal of Dynamical and Control Systems*, 25(3):403–435, 2019.
- [13] T. Breitenbach and A. Borzì. A sequential quadratic hamiltonian scheme for solving non-smooth quantum control problems with sparsity. *Journal of Computational and Applied Mathematics*, 369:112583, 2020.
- [14] A. Dey, A. Borzì, and S. Roy. A high contrast and resolution reconstruction algorithm in quantitative photoacoustic tomography. *Journal of Computational and Applied Mathematics*, page 116065, 2024.
- [15] N. Do, M. Haltmeier, R. Kowar, L. V. Nguyen, and R. Nuster. Full field inversion of the attenuated wave equation: Theory and numerical inversion, 2024.

- [16] P. Elbau, O. Scherzer, and C. Shi. Singular values of the attenuated photoacoustic imaging operator. *J. Differential Equations*, 263(9):5330–5376, 2017.
- [17] L.C. Evans. *Partial Differential Equations*. Graduate studies in mathematics. American Mathematical Society, 2010.
- [18] H. Gao, S. Osher, and H. Zhao. Quantitative Photoacoustic Tomography. *Mathematical Modeling in Biomedical Imaging II, Lecture Notes in Mathematics 2035*, Springer, Heidelberg, pages 131–158, 2012.
- [19] M. Gupta, R. Kumar Mishra, and S. Roy. Sparsity-based nonlinear reconstruction of optical parameters in two-photon photoacoustic computed tomography. *Inverse Problems*, 37(4), 2021.
- [20] M. Gupta, R. K. Mishra, and S. Roy. Sparse reconstruction of log-conductivity in current density impedance tomography. *Journal of mathematical imaging and vision*, 62(2):189–205, 2020.
- [21] M. Gupta, R. K. Mishra, and S. Roy. Sparsity-based nonlinear reconstruction of optical parameters in two-photon photoacoustic computed tomography. *Inverse Problems*, 37(4):044001, 2021.
- [22] M. Haltmeier, T. Berer, S. Moon, and P. Burgholzer. Compressed sensing and sparsity in photoacoustic tomography. *Journal of Optics*, 18(11):114004, 2016.
- [23] M. Haltmeier and L. V Nguyen. Reconstruction algorithms for photoacoustic tomography in heterogeneous damping media. *Journal of Mathematical Imaging and Vision*, 61(7):1007–1021, 2019.
- [24] A. Homan. Multi-wave imaging in attenuating media. *Inverse Problems and Imaging*, 7(4):1235–1250, 2013.
- [25] Y. Hristova, P. Kuchment, and L. Nguyen. Reconstruction and time reversal in thermoacoustic tomography in acoustically homogeneous and inhomogeneous media. *Inverse Problems*, 24(5):055006, aug 2008.
- [26] G. Hwang, G. Jeon, S. Moon, and D. Park. Implicit learning to determine variable sound speed and the reconstruction operator in photoacoustic tomography. *arXiv preprint arXiv:2407.09749*, 2024.
- [27] S. Kim, S. Moon, and I. Seo. Reconstruction of the initial data from the trace of the solutions on an infinite time cylinder of damped wave equations. *Inverse Problems*, 40(6):065009, may 2024.
- [28] C. Knox and A. Moradifam. Determining both the source of a wave and its speed in a medium from boundary measurements. *Inverse Problems*, 36(2):025002, jan 2020.
- [29] R. Kowar and O. Scherzer. Attenuation models in photoacoustics. In *Mathematical modeling in biomedical imaging. II*, volume 2035 of *Lecture Notes in Math.*, pages 85–130. Springer, Heidelberg, 2012.
- [30] P. Kuchment. *The Radon Transform and Medical Imaging*. CBMS-NSF Regional Conference Series in Applied Mathematics. Society for Industrial and Applied Mathematics, 2014.
- [31] H. Liu and G. Uhlmann. Determining both sound speed and internal source in thermo- and photoacoustic tomography. *Inverse Problems*, 31(10):105005, sep 2015.

- [32] M. Moon, I. Hur, and S. Moon. Singular value decomposition of the wave forward operator with radial variable coefficients. *SIAM Journal on Imaging Sciences*, 16(3):1520–1534, 2023.
- [33] A. I. Nachman, J.F. Smith III, and R. C. Waag. An equation for acoustic propagation in inhomogeneous media with relaxation losses. *The Journal of the Acoustical Society of America*, 88(3):1584–1595, 1990.
- [34] L. Nguyen, M. Haltmeier, R. Kowar, and N. Do. Analysis for full-field photoacoustic tomography with variable sound speed. *SIAM Journal on Imaging Sciences*, 15(3):1213–1228, 2022.
- [35] L. Oksanen and G. Uhlmann. Photoacoustic and thermoacoustic tomography with an uncertain wave speed. *Mathematical Research Letters*, 21(5):1199–1214, 2014.
- [36] B. Palacios. Reconstruction for multi-wave imaging in attenuating media with large damping coefficient. *Inverse Problems*, 32(12):125008, nov 2016.
- [37] R. Racke. Lectures on nonlinear evolution equations. *Initial value problems*. Vieweg-Verlag Braunschweig, 2015.
- [38] S. Roy. A new nonlinear sparse optimization framework in ultrasound-modulated optical tomography. *IEEE Transactions on Computational Imaging*, 8:1–11, 2022.
- [39] S. Roy and A. Borzì. A new optimization approach to sparse reconstruction of log-conductivity in acousto-electric tomography. *SIAM Journal on Imaging Sciences*, 11(2):1759–1784, 2018.
- [40] S. Roy, G. Jeon, and S. Moon. Radon transform with gaussian beam: Theoretical and numerical reconstruction scheme. *Applied Mathematics and Computation*, 452:128024, 2023.
- [41] S. Roy and S. Pal. A PINN-driven game-theoretic framework in limited data photoacoustic tomography. *Inverse Problems*, 2025.
- [42] O. Scherzer, editor. *Handbook of Mathematical Methods in Imaging*. Springer, New York, 2 edition, 2015.
- [43] P. Stefanov and G. Uhlmann. Thermoacoustic tomography with variable sound speed. *Inverse Problems*, 25(7):075011, 2009.
- [44] L.V. Wang. *Photoacoustic Imaging and Spectroscopy*. Optical Science and Engineering. Taylor & Francis, 2009.
- [45] G. Zangerl, S. Moon, and M. Haltmeier. Photoacoustic tomography with direction dependent data: an exact series reconstruction approach. *Inverse Problems*, 35(11):114005, oct 2019.